Progress in Physics of Applied Materials 7 (2027), Serial Number 15, 1-8

Semnan University

Progress in Physics of Applied Materials

journal homepage: https://ppam.semnan.ac.ir/

Transfer Matrix Method Analysis of Graphene-Loaded Circular Waveguide

Alireza Dolatabady *, Bahram Rashidi

Department of Electrical Engineering, Faculty of Engineering, Ayatollah Boroujerdi University, Boroujerd, Iran.

ARTICLE INFO

Article history:
Received: 28 April 2026
Revised: 26 July 2026
Accepted: 8 August 2026
Published online: 2 September 2026

Keywords:
Circular waveguide;
Graphene-loaded waveguide;
Photonic band gap;
Transfer matrix method;
Tunable structure.

ABSTRACT

Graphene, owing to its electrically tunable surface conductivity and favorable electromagnetic properties, has attracted considerable attention for microwave and terahertz applications. In this paper, the transfer matrix method is employed to analyze the transmission, reflection, and absorption characteristics of graphene-loaded circular waveguides. Single-layer and periodically arranged non-interacting graphene layers are investigated by incorporating the graphene surface conductivity into the electromagnetic boundary conditions for both TE and TM modes. The effects of the graphene chemical potential and the incident angle on the reflection characteristics are examined for different dielectric configurations. The results show that the electromagnetic response depends on both the polarization and the graphene chemical potential, with the TE mode exhibiting a higher degree of electrical tunability than the TM mode. In addition, the periodic arrangement of graphene layers gives rise to a photonic band gap, whose characteristics are influenced by the graphene chemical potential and the structural parameters. The proposed analytical formulation provides a convenient approach for studying graphene-loaded circular waveguides and may be useful in the analysis and design of tunable microwave and terahertz waveguide components.

1. Introduction

Thanks to the recently developed methods for realizing the ultra-thin structures, two-dimensional materials have attracted considerable interest due to their unique chemical, thermal, mechanical, electrical, and optical features [1]. Graphene, a one-atom-thick layer of carbon atoms arranged in a hexagonal lattice, is regarded as the pioneering material of this generation of materials capable of being employed in a wide variety of photonic devices [2]. Graphene provides several outstanding properties such as high wave confinement [3], high carrier mobility [4], and electro- and magneto-static tunability [5, 6]. So far, various graphene-based components such as waveguides [7], induced transparency window providers [8], logic gates [9], sensors [10, 11], and absorbers [12, 13] have been proposed and investigated. Despite the relatively low rate of absorption (about 2.2% of incident light), single-layer of graphene is considered as a broadband absorber [14]. This feature, in addition to voltage-dependent chemical potential of graphene, has introduced it as a highly promising candidate to be employed in tunable photodetection devices [15]. Moreover, graphene can play a role as a transparent electrode in various opto-electronic systems [16]. Furthermore, a graphene layer can provide remarkable Faraday rotation effect, capable to be utilized in nonreciprocal devices [17]. Owing to these applications, the absorption, reflection, and transmission properties of the single and also, multi-layers of graphene, should be studied.

To utilize graphene layers, various configurations can be employed. Circular waveguides, as a universal type of

* Corresponding author.
E-mail address: alireza.dolatabady@abru.ac.ir

Cite this article as:

Dolatabady, A., and Rashidi, B., 2027. Transfer Matrix Method Analysis of Graphene-Loaded Circular Waveguide. *Progress in Physics of Applied Materials*, *7*(2),pp.1-8. DOI: **10.22075/ppam.2026.41033.1219**

waveguides and compatible with various structures, can possess versatile applications employing the graphene layers [18]. They can be implemented with either metallic or dielectric walls [19]. The widespread usage of optical fibers is one example of the circular dielectric waveguides. So far, various graphene-loaded circular waveguides, either in metallic or dielectric walls, have been investigated, simulated numerically or demonstrated experimentally [18, 20-22]. Therefore, graphene loaded waveguides should be analyzed to establish useful methods for evaluating absorption, reflection, and transmission. One of the simplest and most effective techniques to analyze multi-layer electromagnetic structures is transfer matrix method [23]. To date, numerous studies have been done to study the graphene-based structures using transfer matrix method [24-26].

In this paper, single- and non-interacting multi-layer graphene loaded circular waveguides are considered. An analytical formulation has been developed based on the transfer matrix method to evaluate the coefficients of absorption, reflection, and transmission along the waveguide for two different modes of TE and TM. Through variation of graphene chemical potential, tunability of the reflectance coefficient is explored. Next, the developed transfer matrix formulation is used to investigate a periodic arrangement of graphene layers using Bloch-wave theory [24].

The remainder of this paper is organized as follows: In Section 2, the investigated structures of circular waveguides and the transfer matrix analysis approach are introduced. In Section 3, the reflection, transmission, and absorption properties of the graphene loaded structures are presented. In Section 4, a periodic arrangement of graphene layers is studied. Finally, the paper is concluded in Section 5.

2. The Investigated Structures and Transfer Matrix Analysis Approach

In this section, the transfer matrix method is employed to analyze single- and multi-layer graphene-loaded circular metallic waveguides. According to this method, the electric or magnetic fields of the forward- and backward-propagating waves on one side of a medium are expressed in terms of those on the opposite side. The overall transfer matrix of the structure is obtained by multiplying a series of submatrices, which are generally classified into transmission and propagation matrices. These matrices are derived for the investigated structure as follows:

2.1. Transmission Matrix

The transmission matrix is derived based on the structure shown in Fig. 1, where a circular waveguide is loaded with a single graphene layer that divides the dielectric region into two media with permittivities ε_1 and ε_2 and permeabilities of μ_1 and μ_2. The graphene layer, located at z=0, is characterized by its surface conductivity, which is described by the well-known Kubo formula [4]:

$$\begin{aligned}\sigma &= -j\frac{e^2 k_B T}{\pi\hbar^2(\omega - j\tau^{-1})}\left\{\frac{\mu_c}{k_B T} + 2\,ln\left[exp\left(-\frac{\mu_c}{k_B T}\right)+1\right]\right\} \\ &\quad - j\frac{e^2}{4\pi\hbar^2}ln\left[\frac{2|\mu_c| - \hbar(\omega - j\tau^{-1})}{2|\mu_c| + \hbar(\omega - j\tau^{-1})}\right] \end{aligned} \tag{1}$$

where j, e, k_B, T, τ, μ_c, ω, and $\hbar$, denote imaginary unit, electron charge, Boltzmann constant, temperature, carrier relaxation time, chemical potential, angular frequency, and reduced Planck constant, respectively. For highly doped graphene at room temperature and operating in the terahertz frequency range, the graphene surface conductivity can be simplified as [4]:

$$\sigma = \frac{-je^2\mu_c}{\pi\hbar^2(\omega - j\tau^{-1})} \tag{2}$$

The transmission matrix is derived from the relationship between the incident and reflected waves at the graphene interface between the two ports of the circular waveguide shown in Fig. 1(a). The electromagnetic waves are analyzed for the two fundamental polarizations, namely TE and TM, propagating along the (z)-direction. For the TE mode, according to electromagnetic theory and for the structure shown in Fig. 1(a), which consists of two dielectric media surrounding the graphene layer and denoted by (1) and (2), the total electric and magnetic fields can be expressed as follows [19]:

$$\boldsymbol{E}_i = \left(E_{i\rho+} + E_{i\rho-}\right)\boldsymbol{a}_\rho + \left(E_{i\varphi+} + E_{i\varphi-}\right)\boldsymbol{a}_\varphi \tag{3}$$

$$\begin{aligned}\boldsymbol{H}_i = \left(H_{i\rho+} + H_{i\rho-}\right)\boldsymbol{a}_\rho + \left(H_{i\varphi+} + H_{i\varphi-}\right)\boldsymbol{a}_\varphi \\ + \left(H_{iz+} + H_{iz-}\right)\boldsymbol{a}_z\end{aligned} \tag{4}$$

where, $F_{i\rho+(-)}, F_{i\varphi+(-)}, F_{iz+(-)}$ (F=E or H, i=1, 2) denote radial, azimuthal, and longitudinal components of the electric or magnetic field in ith medium, respectively. The subscripts of + and – refer to the direction along +z and –z, respectively. For a circular waveguide, the following relations hold [19]:

$$\begin{aligned}E_{i\rho+(-)} = -A_{imn}^{+(-)}\frac{m}{\varepsilon_i\rho}J_m\left(\beta_{i\rho}\rho\right)[-C_i\,sin(m\varphi) \\ + D_i\,cos(m\varphi)]e^{-(+)j\beta_{iz}z}\end{aligned} \tag{5}$$

$$\begin{aligned}E_{i\varphi+(-)} = A_{imn}^{+(-)}\frac{\beta_{i\rho}}{\varepsilon_i}J'_m\left(\beta_{i\rho}\rho\right)[C_i\,cos(m\varphi) \\ + D_i\,sin(m\varphi)]e^{-(+)j\beta_{iz}z}\end{aligned} \tag{6}$$

and:

$$\begin{aligned}E_{i\rho+(-)} = -A_{imn}^{+(-)}\frac{m}{\varepsilon_i\rho}J_m\left(\beta_{i\rho}\rho\right)[-C_i\,sin(m\varphi) \\ + D_i\,cos(m\varphi)]e^{-(+)j\beta_{iz}z}\end{aligned} \tag{7}$$

$$E_{i\varphi+(-)} = A^{+(-)}_{imn}\frac{\beta_{i\rho}}{\varepsilon_i}J'_m(\beta_{i\rho}\rho)[C_i\, cos(m\varphi) + D_i\, sin(m\varphi)]e^{-(+)j\beta_{iz}z} \quad (8)$$

where m, n=0, 1, ..., denote the mode indices and A~D represent the field amplitudes. $J(\cdot)$ denotes the Bessel function of the first kind. The propagation constant is denoted by β such that $\beta_{i\rho}^2 + \beta_{iz}^2 = \omega^2\mu_i\varepsilon_i$. The following boundary conditions must be satisfied to relate the electric and magnetic fields at the interface z=0:

$$\boldsymbol{a}_z \times (\boldsymbol{E}_2 - \boldsymbol{E}_1)|_{z=0} = 0 \quad (9)$$

$$\boldsymbol{a}_z \times (\boldsymbol{H}_2 - \boldsymbol{H}_1)|_{z=0} = \boldsymbol{J}_s \quad (10)$$

where $\mathbf{J}_s$ denotes for surface current density on the graphene layer, proportional to tangential electric field, $\mathbf{E}_t$, through Ohm's law, as:

$$\boldsymbol{J}_s = \sigma\boldsymbol{E}_t \quad (11)$$

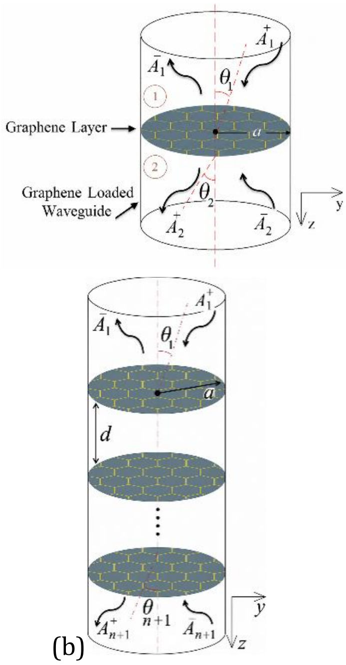

Fig. 1. (a) Single-layer and (b) multi-layer graphene loaded circular waveguides.

Hence, the following relation is obtained:

$$\frac{1}{\varepsilon_1}(A^+_{1mn} + A^-_{1mn}) = \frac{1}{\varepsilon_2}(A^+_{2mn} + A^-_{2mn}) \quad (12)$$

and:

$$\left(\frac{\beta_{1z}}{\omega\mu_1\varepsilon_1}\right)(-A^+_{1mn} + A^-_{1mn}) = \left(\frac{\beta_{2z}}{\omega\mu_2\varepsilon_2} + \frac{\sigma}{\varepsilon_2}\right)(-A^+_{2mn}) + \left(\frac{\beta_{2z}}{\omega\mu_2\varepsilon_2} - \frac{\sigma}{\varepsilon_2}\right)(A^-_{2mn}) \quad (13)$$

The above equations can be combined into the following matrix equation which relates A^+_{1mn} and A^-_{1mn} to A^+_{2mn} and A^-_{2mn} through a 2×2 transmission matrix $\mathbf{B}_{1\to2}$:

$$\begin{bmatrix} A^+_{1mn} \\ A^-_{1mn} \end{bmatrix} = \boldsymbol{B}_{1\to2}\begin{bmatrix} A^+_{2mn} \\ A^-_{2mn} \end{bmatrix} \quad (14)$$

where:

$$\boldsymbol{B}_{1\to2} = \frac{\mu_1\varepsilon_1}{2\beta_{1z}\varepsilon_2}\begin{bmatrix} B_{11} & B_{12} \\ B_{21} & B_{22} \end{bmatrix} \quad (15)$$

In Eq. (15), $B_{11} = \frac{\beta_{1z}}{\mu_1} + \frac{\beta_{2z}}{\mu_2} + \sigma\omega$, $B_{12} = \frac{\beta_{1z}}{\mu_1} - \frac{\beta_{2z}}{\mu_2} + \sigma\omega$, $B_{21} = \frac{\beta_{1z}}{\mu_1} - \frac{\beta_{2z}}{\mu_2} - \sigma\omega$, and $B_{22} = \frac{\beta_{1z}}{\mu_1} + \frac{\beta_{2z}}{\mu_2} - \sigma\omega$. Equation (14) describes the relationship between the incident, reflected, and transmitted TE waves propagating along the z-direction in a circular waveguide, consisting of two media separated by the interface at z=0.

Using the same procedure, we can find the transmission matrix for TM polarization:

$$E_{i\rho+(-)} = -A^{+(-)}_{imn}\frac{\beta_{i\rho}\beta_{iz}}{\omega\mu_i\varepsilon_i}J'_m(\beta_{i\rho}\rho)[C_i\, cos(m\varphi) + D_i\, sin(m\varphi)]e^{-(+)j\beta_{iz}z} \quad (16)$$

$$E_{i\varphi+(-)} = -A^{+(-)}_{imn}\frac{m\beta_{iz}}{\omega\mu_i\varepsilon_i\rho}J_m(\beta_{i\rho}\rho)[-C_i\, sin(m\varphi) + D_i\, cos(m\varphi)]e^{-(+)j\beta_{iz}z} \quad (17)$$

and:

$$H_{i\rho+(-)} = \frac{+}{(-)}A^{+(-)}_{imn}\frac{m}{\mu_i\rho}J_m(\beta_{i\rho}\rho)[-C_i\, sin(m\varphi) + D_i\, cos(m\varphi)]e^{-(+)j\beta_{iz}z} \quad (18)$$

$$H_{i\varphi+(-)} = \frac{-}{(+)}A^{+(-)}_{imn}\frac{\beta_{i\rho}}{\mu_i}J'_m(\beta_{i\rho}\rho)[C_i\, cos(m\varphi) + D_i\, sin(m\varphi)]e^{-(+)j\beta_{iz}z}, \quad (19)$$

After imposing the appropriate boundary conditions, following the same procedure used for the TE polarization to obtain Eq. (15), the following relation is obtained:

$$\frac{1}{\mu_1\varepsilon_1}(A^+_{1mn} + A^-_{1mn}) = \frac{1}{\mu_2\varepsilon_2}(A^+_{2mn} + A^-_{2mn}) \quad (20)$$

$$\left(\frac{1}{\mu_1}\right)(-A^+_{1mn} + A^-_{1mn}) = \left(\frac{\sigma\beta_{2z}}{\omega\mu_2\varepsilon_2} + \frac{1}{\mu_2}\right)(-A^+_{2mn}) + \left(-\frac{\sigma\beta_{2z}}{\omega\mu_2\varepsilon_2} + \frac{1}{\mu_2}\right)(A^-_{2mn}) \quad (21)$$

Hence, the following matrix equation is obtained:

$$\boldsymbol{B}_{1\to2} = \frac{\varepsilon_1}{2}\begin{bmatrix} B_{11} & B_{12} \\ B_{21} & B_{22} \end{bmatrix} \quad (22)$$

where:

$B_{11} = \frac{\mu_1}{\mu_2}\left(\frac{1}{\varepsilon_2} + \frac{1}{\varepsilon_1}\left(\frac{\sigma\beta_{2z}}{\omega\varepsilon_2} + 1\right)\right)$, $B_{12} = \frac{\mu_1}{\mu_2}\left(\frac{1}{\varepsilon_2} + \frac{1}{\varepsilon_1}\left(\frac{\sigma\beta_{2z}}{\omega\varepsilon_2} - 1\right)\right)$, $B_{21} = \frac{\mu_1}{\mu_2}\left(\frac{1}{\varepsilon_2} - \frac{1}{\varepsilon_1}\left(\frac{\sigma\beta_{2z}}{\omega\varepsilon_2} + 1\right)\right)$, and

$$B_{22} = \frac{1}{\varepsilon_2} + \frac{1}{\varepsilon_1}\left(\frac{-\sigma\beta_{2z}}{\omega\varepsilon_2} + 1\right).$$

2.2. Propagation Matrix

Next, wave propagation in the ith homogeneous medium along the z-axis is considered. The transmitted electric and magnetic fields can be obtained after propagation through a distance of di, by applying the following matrix [27]:

$$\boldsymbol{P}_i = \begin{bmatrix} exp(-j\beta_{iz}d_i) & 0 \\ 0 & exp(j\beta_{iz}d_i) \end{bmatrix} \tag{23}$$

2.3. Total Transfer Matrix for a Multi-layer Graphene Loaded Waveguide

Consider the structure shown in Fig. 1(b) with N successive graphene layers. Assuming that the first graphene layer is located at z=0, the overall transfer matrix of the structure is obtained by multiplying transmission matrices of graphene layers and propagation matrices of the intermediate homogeneous media (the media labeled 2, 3, ...) [24]:

$$\boldsymbol{T} = \boldsymbol{B}_{(1\to2)}\boldsymbol{P}_2\boldsymbol{B}_{(2\to3)}\boldsymbol{P}_3 \ldots \tag{24}$$

Therefore, the following relation holds between the field amplitudes of A^{+}_{1mn} and A^{-}_{1mn} in the first medium and A^{+}_{N+1mn} and A^{-}_{N+1mn} in the last medium [24]:

$$\begin{bmatrix} A^{+}_{1mn} \\ A^{-}_{1mn} \end{bmatrix} = \boldsymbol{T}\begin{bmatrix} A^{+}_{N+1mn} \\ A^{-}_{N+1mn} \end{bmatrix} \tag{25}$$

3. Transmission, Reflection, and Absorption

To analyze the transmission, reflection, and absorption characteristics, the scattering matrix, is introduced which relates the incoming waves to the outgoing waves. For the multi-layer graphene-loaded waveguide shown in Fig. 1(b), the scattering matrix can be expressed as [28]:

$$\begin{bmatrix} A^{-}_{1mn} \\ A^{+}_{N+1mn} \end{bmatrix} = \boldsymbol{S}\begin{bmatrix} A^{+}_{1mn} \\ A^{-}_{N+1mn} \end{bmatrix} \tag{26}$$

It can also be shown that:

$$\boldsymbol{S} = \begin{bmatrix} \frac{T_{21}}{T_{11}} & \frac{(T_{11}T_{22} - T_{12}T_{21})}{T_{11}} \\ \frac{1}{T_{11}} & \frac{-T_{12}}{T_{11}} \end{bmatrix} \tag{27}$$

where T_{ij} (i,j=1,2) are the elements of **T**. Therefore, the reflection (r) and transmission (t) coefficients are given by:

$$r = \frac{T_{21}}{T_{11}}, t = \frac{1}{T_{11}} \tag{28}$$

The corresponding reflectance (R), transmittance (T), and absorbance (A) are then calculated as:

$$R = |r|^2, T = \eta|t|^2, A = 1 - R - T \tag{29}$$

The values of parameters in Eq. (29) are obtained from the corresponding polarization-dependent transfer matrices.

3.1. TE Polarization

For TE polarization, the reflectance and transmittance of Eq. (29) in a non-magnetic medium (i.e. $\mu_1 = \mu_2 = \mu_0$) can be expressed as:

$$R = \left|\frac{\sqrt{\varepsilon_{r1}}\cos\theta_1 - \sqrt{\varepsilon_{r2}}\cos\theta_2 - \sigma\eta_0}{\sqrt{\varepsilon_{r1}}\cos\theta_1 + \sqrt{\varepsilon_{r2}}\cos\theta_2 + \sigma\eta_0}\right|^2 \tag{30}$$

$$T = Z^{TE}_{mn}\left|\frac{\eta_0}{\omega[\sqrt{\varepsilon_{r1}}\cos\theta_1 + \sqrt{\varepsilon_{r2}}\cos\theta_2 + \eta_0\sigma]}\right|^2 \tag{31}$$

where η_0, denotes the free-space wave impedance. θ_1 and θ_2 are, respectively, the incident and refracted angles, related through Snell's law. $Z^{TE}_{mn} = \frac{\omega\mu}{\beta_z} = \frac{\eta_0}{\sqrt{\varepsilon_{r1}}\cos\theta_1}$ is wave impedance for mnth order mode of TE wave. ε_{ri} is relative permittivity in the ith medium.

3.2. TM Polarization

Similarly, for the TM polarization, Eq. (30) and (31) would be changed as:

$$R = \left|\frac{\varepsilon_1 - \left(\frac{\sigma}{c}\sqrt{\varepsilon_{r2}}\cos\theta_2 + \varepsilon_2\right)}{\varepsilon_1 + \left(\frac{\sigma}{c}\sqrt{\varepsilon_{r2}}\cos\theta_2 + \varepsilon_2\right)}\right|^2 \tag{32}$$

$$T = Z^{TM}_{mn}\left|\frac{\varepsilon_1\varepsilon_2}{\varepsilon_1 + \frac{\sigma}{c}\sqrt{\varepsilon_{r2}}\cos\theta_2 + \varepsilon_2}\right|^2 \tag{33}$$

where $Z^{TM}_{mn} = \frac{\beta}{\omega\varepsilon} = \frac{\eta_0}{\sqrt{\varepsilon_{r1}}}\cos\theta_1$ is wave impedance for mnth order mode of TM wave. It should be noted that in both TE and TM polarizations, θ depends on the waveguide mode, as it is usual in waveguide modes.

Fig. 2 illustrates the reflectance of a single-layer graphene-loaded circular waveguide as a function of the incident angle, for two different polarizations of TE and TM, in a non-homogenous medium (i.e. $\varepsilon_1 \neq \varepsilon_2$). Two different cases of wave transmission from the media with lower relative permittivity toward higher relative permittivity, and vice versa, are considered. The physical parameters of the graphene layer and the structural parameters of the investigated structure shown in Fig. 1(b), are summarized in Table 1.

Fig. 2 demonstrates the strong dependence of the reflectance on the incident angle for both TE and TM polarizations. For the TE mode, the reflectance increases gradually from approximately 0.89 at normal incidence to nearly unity as the incident angle approaches 90°, whereas for the TM mode it remains close to unity below the critical angle and then decreases sharply to almost zero before slightly recovering to about 0.15 at larger incident angles. These results indicate that the waveguide exhibits a highly polarization-dependent angular response.

Fig. 3 shows the reflectance of a single-layer graphene-loaded circular waveguide presented as a three-dimensional surface plot, as a function of the chemical potential and the incident angle.

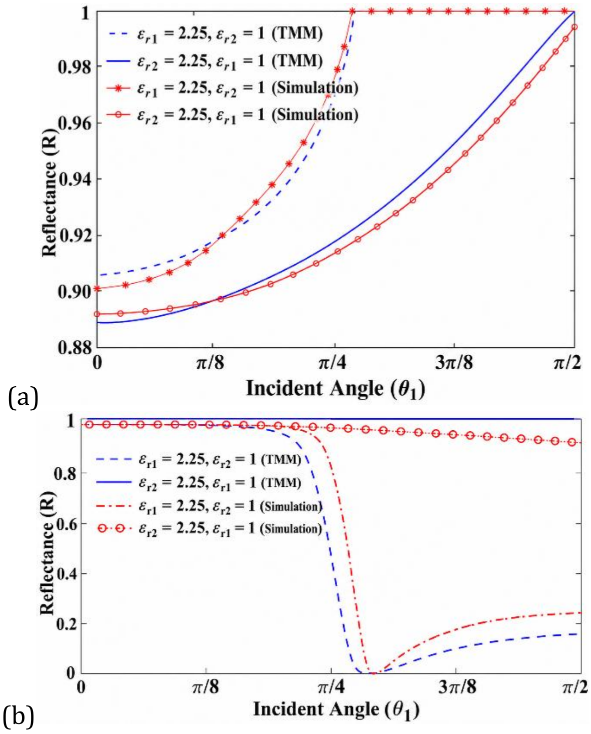

Fig. 2. Reflectance of a single-layer graphene-loaded circular waveguide versus incident angle for *f*=1 THz, for (a) TE and (b) TM polarizations. Solid blue curves indicate wave transmission from the media with lower relative permittivity toward higher relative permittivity, and dashed blue curves vice versa, based on transfer matrix method. The red curves are based on the simulation results.

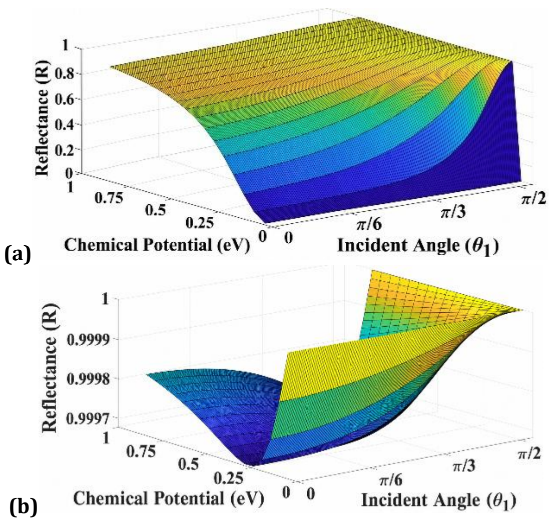

Fig. 3. Reflectance of a single-layer graphene-loaded circular waveguide in a three-dimensional curve, versus chemical potential and incident angle for (a) TE and (b) TM polarizations.

Table 1. Physical parameters of the graphene layer and the structural parameters of the investigated structure shown in Fig. 1(b).

τ (*ns*)	μ_c (eV)	f=ω/2π (THz)	*T* (K)	*a* (μm)	*d* (μm)
1	1	1	300	100	20

Fig. 3 illustrates the combined influence of the graphene chemical potential and the incident angle on the reflectance. For the TE polarization, increasing the chemical potential enhances the reflectance over a wide range of incident angles, with the largest tunability occurring near the critical angle. In contrast, the TM polarization exhibits only a slight variation with chemical potential, indicating that the TE mode provides a significantly higher degree of electrical tunability.

3.3. Double-Layer Graphene

Based on the multi-layer graphene configuration in Fig. 1(b), a double-layer graphene loaded circular waveguide is considered. The two graphene layers are separated by a distance d. Therefore, the non-magnetic medium is divided into three distinct media with permittivities εi (i=1~3). So, the overall transfer matrix of the structure is obtained as:

$$\boldsymbol{T} = \boldsymbol{B}_{(1\to2)}\boldsymbol{P}_2\boldsymbol{B}_{(2\to3)} \tag{34}$$

Fig. 4 illustrates reflectance and transmittance of a double-layer graphene loaded circular waveguide as functions of the incident angle for both TE and TM polarizations. The physical parameters of the two graphene layers are assumed to be identical.

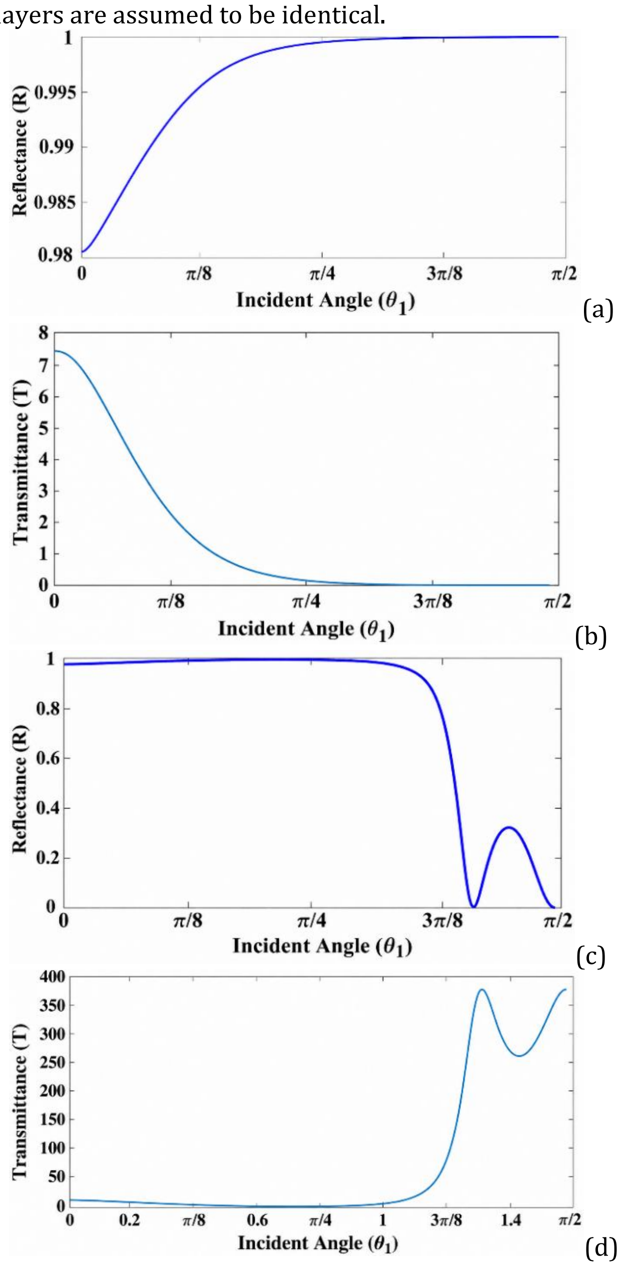

Fig. 4. Reflectance and transmittance for double-layer graphene-loaded circular waveguide in homogenous media ($\varepsilon_1 \neq \varepsilon_2$) versus incident angle for (a)-(b) TE and (c)-(d) TM polarizations.

Fig. 4 shows the angular dependence of the reflectance and transmittance for a double-layer graphene-loaded circular waveguide. For the TE polarization, the reflectance increases from about 0.99 to nearly unity as the incident angle increases, while the transmittance decreases correspondingly from approximately 8% to nearly zero, demonstrating excellent reflection at large incident angles. For the TM polarization, both the reflectance and transmittance exhibit pronounced angular variations around the critical angle, confirming the strong polarization-selective behavior of the proposed structure.

In our investigation, the graphene layers behave non-interacting because they are separated by dielectric layers sufficiently thick to neglect direct near-field electromagnetic coupling and quantum tunneling between adjacent sheets. Consequently, each graphene layer is modeled as an independent conductive interface characterized solely by its surface conductivity within the transfer matrix formulation.

The different sensitivities of the TE and TM polarizations to the graphene chemical potential and the incident angle originate from their distinct electromagnetic boundary conditions at the graphene interface. In the TE mode, the tangential electric field directly couples to the graphene surface conductivity, making the reflection and transmission coefficients more sensitive to variations in the chemical potential. Since the graphene conductivity increases with chemical potential, the effective surface impedance decreases, resulting in stronger reflection and enhanced tunability. In contrast, the TM mode is governed by a different field configuration, in which the magnetic field and the normal electric-field components play a more significant role. Consequently, the contribution of the graphene surface conductivity to the overall wave impedance is less pronounced, leading to weaker sensitivity to changes in the chemical potential.

Furthermore, at an operating frequency of 1 THz, the graphene conductivity is dominated by the intraband (Drude-like) contribution, while the interband contribution remains negligible because the photon energy is much smaller than twice the chemical potential. Under these conditions, the conductivity is predominantly inductive, with a large imaginary part and a relatively small real part. As a result, changing the chemical potential primarily modifies the reactive surface impedance of graphene rather than introducing significant absorption. This behavior explains the pronounced tunability of the reflectance, particularly for the TE polarization, while the incident angle further influences the propagation constants and wave impedance of both polarizations, thereby altering the coupling efficiency at the graphene interface and shifting the angular response observed in Figs. 2–4.

3.4. Numerical Validation

To confirm the accuracy and reliability of the developed analytical Transfer Matrix Method formulation, we used Comsol software package. To accomplish the simulation, we modeled the circular waveguide, replaced graphene by a surface conductivity boundary and computed the reflection coefficient. The structural parameters were summarized in Table 1. We just simulated the operation of the single layer structure of Figure 1(a) numerically. In Figures 2(a) and (b), the simulation results are shown in red. There is a good agreement between the results based on the transfer matrix method and simulation. According to Figure 2(a), for the TE polarization, when the incident wave propagates from the higher-permittivity medium (ε_{r1}=2.25) toward the lower-permittivity medium (ε_{r2}=1), the reflectance rapidly approaches unity near the critical angle due to the onset of total internal reflection. In contrast, for the reverse dielectric configuration, no critical angle exists, and the reflectance increases gradually with incident angle as a result of the increasing TE wave impedance. These observations confirm both the physical consistency of the model and the accuracy of the developed transfer matrix analysis. In Figure 2(b), for TM polarization, the reflectance decreases with increasing incident angle and reaches a pronounced minimum due to an impedance-matching condition established between the dielectric interface and the graphene surface conductivity. This behavior is analogous to a generalized Brewster effect, whose position is modified by the graphene-induced surface impedance. Beyond this angle, the impedance mismatch increases again, leading to a gradual recovery of the reflectance.

For the metallic circular waveguide, the dominant TE_{11} mode has the following cutoff frequency [28]:

$$f_c = \frac{1.841c}{2\pi a\sqrt{\varepsilon_r}} \tag{35}$$

where for an air-filled waveguide, ε_r=1. Rearranging the cutoff formula for f_c=1 THz gives, yields a≈88 μm. To ensure good propagation at 1 THz, the operating frequency should be comfortably above cutoff. A practical choice can therefore be a=100 μm. This is the radius of the circular waveguide used in the numerical simulations. For this radius, the cutoff frequencies of the investigated TE and TM modes are below the operating frequency of 1 THz, ensuring that the considered modes propagate inside the waveguide rather than existing in the evanescent regime.

4. Photonic Band Gap for a Periodic Arrangement of Graphene Layers

Graphene layers can be arranged in a periodic configuration, to create photonic crystal structures, as shown in Figs. 5(a) and (b), for one- and two-part unit cell periodic structures. For a two-part structure, supposing the identical graphene layers, the transfer matrix over propagation along one unit cell can be calculated as:

$$\boldsymbol{T} = \boldsymbol{B}_{(1\to 2)}\boldsymbol{P}_2\boldsymbol{B}_{(2\to 1)}\boldsymbol{P}_1 \tag{36}$$

Therefore, by considering the diagonal elements of the transfer matrix, the photonic band gap can be calculated by the following relation [25]:

$$cos(qd) = \frac{trace(\boldsymbol{T})}{2} = \frac{(T_{11} + T_{22})}{2} \tag{37}$$

where q denotes Bloch wavenumber and d=d_1+d_2, so called the lattice constant. Regarding $\boldsymbol{B}_{(2\to 1)} = \boldsymbol{B}_{(1\to 2)}^{-1}$, Eq. (37) leads to the following for both TE and TM modes:

$$cos(qd) = \frac{B_{11}B_{22}\,cos(\beta_{z1}d_1 + \beta_{z2}d_2) - B_{12}B_{21}\,cos(\beta_{z2}d_2 - \beta_{z1}d_1)}{B_{11}B_{22} - B_{12}B_{21}} \tag{38}$$

where B_{ij}, are defined in Eqs. (15) and (22), for TE and TM modes, respectively. Figures 5(c) and (d) show the photonic band structure of the periodic graphene-loaded circular waveguides of Figs. 5(a) and (b) obtained by combining the transfer matrix method with Bloch's theorem. The transfer matrix of one unit cell is first constructed and the corresponding Bloch wave vector is determined from the dispersion relation derived in Eq. (37). By evaluating this relation over the frequency range of interest, the band diagram is generated by plotting the normalized Bloch wave vector, $\frac{qd}{\pi}$, versus normalized frequency, $\frac{\hbar\omega}{\mu_c}$. Frequency regions satisfying $|trace(\mathbf{T})/2| \leq 1$ correspond to propagating Bloch modes (allowed bands), whereas $|trace(\mathbf{T})/2| > 1$ indicates a complex Bloch wave vector, resulting in evanescent waves and the formation of photonic band gaps. The position and width of the band gaps can be effectively tuned by varying the graphene chemical potential. Furthermore, the band structure depends on the dielectric properties, lattice period, waveguide dimensions and the angle of incidence through the propagation constants of the TE and TM modes.

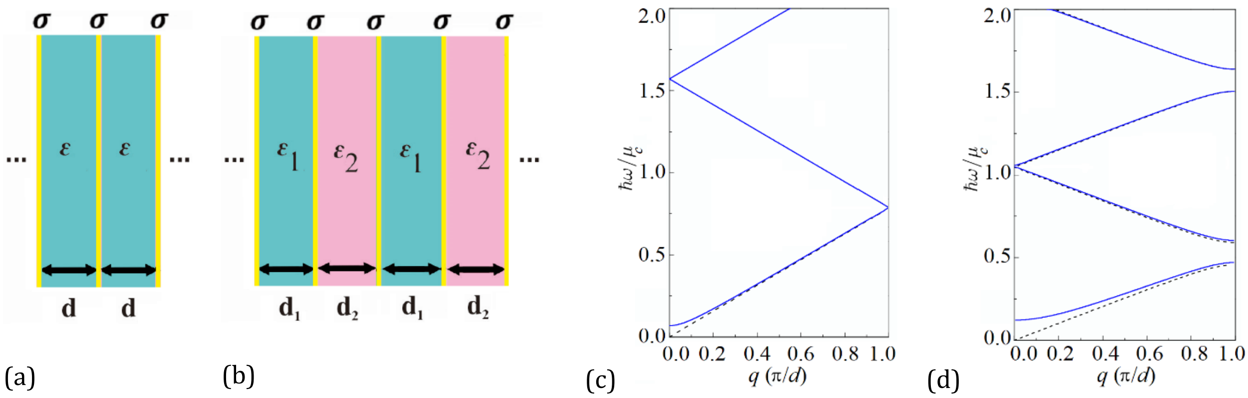

Fig. 5. (a) One- and (b) two-part unit cell periodic structures including two-layer configuration loaded in circularly waveguide considered in Section 4. (c) and (d) are the corresponding photonic band structures obtained for the configurations of (a) and (b), respectively.

As shown in Figure 5(c), the one-part unit cell periodic graphene-loaded structure exhibits a distinct photonic band gap extending over the approximate normalized frequency range $0.8 \leq \frac{\hbar\omega}{\mu_c} \leq 1.6$. The location and width of this forbidden frequency region are determined by the dispersion characteristics of the periodic structure and can be further engineered through the graphene chemical potential and the lattice period, providing an effective mechanism for tunable terahertz filtering.

5. Conclusions

In this paper, the transfer matrix method was employed to investigate the electromagnetic response of single- and non-interacting multilayer graphene-loaded circular waveguides. Analytical formulations were developed for both TE and TM modes by incorporating the graphene surface conductivity into the modified boundary conditions. The proposed model was further extended to periodic graphene-loaded structures to analyze their photonic band-gap characteristics. The results demonstrated that the reflection, transmission, and absorption characteristics can be effectively controlled by varying the graphene chemical potential and the incident angle. The TE polarization exhibited significantly higher electrical tunability than the TM polarization, with the reflectance increasing from approximately 0.9 to nearly unity under suitable operating conditions. Moreover, the one-part unit cell periodic graphene-loaded structure exhibited a distinct photonic band gap over the normalized frequency range of $0.8 \leq \frac{\hbar\omega}{\mu_c} \leq 1.6$ whose position and width can be engineered through the graphene chemical potential and the lattice period. These findings demonstrate the potential of the proposed structure for reconfigurable microwave and terahertz filters, modulators, waveguide components, and highly sensitive sensing applications.

Funding Statement

This research received no specific grant from any funding agency.

Conflicts of Interest

The authors declare that they have no known competing financial interests or personal relationships that could have appeared to influence the work reported in this paper.

Authors' Contribution Statement

Author 1: Conceptualization and study design, manuscript writing and editing, and also, supervision and project administration.
Author 2: Plotting and visualization of the results.
All authors have read and approved the final version of the manuscript.

References

[1] Yu, T. and Breslin, C.B., 2020. Review-2D graphene and graphene-like materials and their promising applications in the generation of hydrogen peroxide. *Journal of The Electrochemical Society*, *167*, p. 126502.

[2] Kalami, A. and Ketabi, S.A., 2021. Spin-dependent thermoelectric properties of a magnetized zigzag graphene

nanoribbon. *Progress in Physics of Applied Materials*, *1*(1), pp. 1-6.

[3] Fan, Y., Shen, N.H., Zhang, F., Zhao, Q., Wu, H., Fu, Q., Wei, Z., Li, H. and Soukoulis, C.M., 2019. Graphene plasmonics: A platform for 2D optics. *Advanced Optical Materials*, *7*, p. 1800537.

[4] Li, H.J., Wang, L.L., Sun, B., Huang, Z.R. and Zhai, X., 2014. Controlling mid-infrared surface plasmon polaritons in the parallel graphene pair. *Applied Physics Express*, *7*, p. 125101.

[5] Dolatabady, A. and Granpayeh, N., 2019. Graphene based far-infrared junction circulator. *IEEE Transactions on Nanotechnology*, *18*, pp. 200-207.

[6] Dolatabady, A. and Granpayeh, N., 2019. Manipulation the Faraday rotation by graphene metasurfaces. *Journal of Magnetism and Magnetic Materials*, *469*, pp. 231-235.

[7] Dolatabady, A., Granpayeh, N. and Salehi, M., 2018. Ferrite loaded graphene based plasmonic waveguide. *Optical and Quantum Electronics*, *50*, p. 345.

[8] Dolatabady, A. and Granpayeh, N., 2018. Tunable far-infrared plasmonically induced transparency in graphene based nano-structures. *Journal of Optics*, *20*, p. 075001.

[9] Dolatabady, A. and Granpayeh, N., 2020. Frequency-tunable logic gates in graphene nano-waveguides. *Photonic Network Communications*, *39*(3), pp. 187-194.

[10] Nasiri, M.A., Rezaei, P., Khani, S. and Khatami, S.A., 2026. High-sensitive graphene-based biosensor for label-free refractive index detection of breast cancer cells. *Results in Optics*, *24*, p. 101064.

[11] Hadipour, S., Rezaei. P. and Khani, S., 2026. Broadband configurable perfect absorber based on surface patterned graphene sheet in THz region. *Results in Optics*, *24*, p. 101010.

[12] Khani, S., Rezaei, P. and Rahmanimanesh, M., 2025. Single-narrowband graphene-based metamaterial absorber for bio-sensing applications with absorption prediction using machine learning analysis. *Results in Engineering*, *28*, p. 107821.

[13] Daraei, OM., Rezaei, P., Khatami, S.A., Zamzam, P., Mohapatra, S., Appasani, B. and Khani, S., 2025. Absorption bandwidth enhancement technique using stacked unequal cross-shaped graphene absorber. *Results in Optics*, *21*, p. 100872.

[14] Yao, G., Ling, F., Yue, J., Luo, C., Luo, Q. and Yao, J., 2016. Dynamically electrically tunable broadband absorber based on graphene analog of electromagnetically induced transparency. *IEEE Photonics Journal*, *8*, p. 7800808.

[15] Liu, C.H., Chang, Y.C., Norris, T.B. and Zhong, Z., 2014. Graphene photodetectors with ultra-broadband and high responsivity at room temperature. *Nature Nanotechnology Letter*, *9*, pp. 273-278.

[16] Kuzum, D., Takano, H., Shim, E., Reed, J.C., Juul, H., Richardson, A.G., de Vries, J., Bink, H., Dichter, M.A., Lucas, T.H., Coulter, D.A., Cubukcu, E. and Litt, B., 2014. Transparent and flexible low noise graphene electrodes for simultaneous electrophysiology and neuroimaging. *Nature Communications*, *5*, p. 5259.

[17] Fallahi, A. and Carrier, J.P., 2012. Manipulation of giant Faraday rotation in graphene metasurfaces. *Applied Physics Letter*, *101*, p. 231605.

[18] Sounas, D.L., Skulason, H.S., Nguyen, H.V., Guermoune, A., Siaj, M., Szkopek, T. and Caloz, C., 2013. Faraday rotation in magnetically biased graphene at microwave frequencies. *Applied Physics Letter*, *102*, p. 191901.

[19] Balanis, C.A., 2012. *Advanced Engineering Electromagnetics*. Wiley.

[20] Bao, Q., Zhang, H., Wang, B., Ni, Z., Lim, C.H.Y.X., Wang, Y., Tang, D.Y. and Loh, K.P., 2011. Broadband graphene polarizer. *Nature Photonics Letter*, *5*, pp. 411-415.

[21] Sounas, D.L. and Caloz, C., 2012. Gyrotropy and nonreciprocity of graphene for microwave applications. *IEEE Transactions on Microwave Theory and Techniques*, *60*, pp. 901-914.

[22] Xiao, B., Sun, R., Xie, Z., Kong, S. and Wang, X., 2017. A Faraday isolator based on graphene. *Optik*, *134*, pp. 60-65.

[23] Katsidis, C.C. and Siapkas, D.I., 2002. General transfer-matrix method for optical multilayer systems with coherent, partially coherent, and incoherent interference. *Applied Optics*, *41*, pp. 3978-3987.

[24] Zhan, T., Shi, X., Dai, Y., Liu, X. and Zi, J., 2013. Transfer matrix method for optics in graphene layers. *Journal of Condensed Matter*, *25*, p. 215301.

[25] Deng, X.H., Liu, J.T., Yuan, J.R., Liao, Q.H. and Liu, N.H., 2015. A new transfer matrix method to calculate the optical absorption of graphene at any position in stratified media. *Europhysics Letter*, *109*, p. 27002.

[26] Li, H., Wang, L., Lan, Z. and Zheng, Y., 2009. Generalized transfer matrix theory of electronic transport through a graphene waveguide. *Physics Review B*, 79, p. 155429.

[27] Yeh, P., 1998. *Optical Waves in Layered Media*. Wiley.

[28] Pozar, D.M., 2012. *Microwave Engineering*. Wiley.arrays. *ACS Applied Materials & Interfaces*, *16*(1), pp.1259–1267.